Fracture deformation and influence on permeability

V. V. Mourzenko,* O. Galamay,* and J.-F. Thovert
Phénomènes de Transport dans les Mélanges/Laboratoire de Combustion et Détonique, SP2MI, Boulevard 3, Téléport 2, 86960 Futuroscope Cedex, France

P. M. Adler
Institut de Physique du Globe de Paris, Tour 24, 4 Place Jussieu, 75252 Paris Cedex 05, France
(Received 2 December 1996)

One of the simplest aspects of coupling between mechanics and hydromechanics of fractures is addressed by the numerical resolution of the mechanical and hydrodynamic equations in three dimensions at the local level. A mean field approximation is derived that may include nonlinear effects because of the variations of the contact surface. Three types of fractures were studied, namely, model deterministic, Gaussian, and self-affine. Numerical results relative to the closure of the fracture, the normal stiffness, and the permeability are presented and discussed. They are satisfactorily compared to available experimental results. [S1063-651X(97)16108-6]

PACS number(s): 83.50.−v

I. INTRODUCTION

The major purpose of this paper is to study the deformation of fractures under normal loads and to determine the resulting changes in permeability. Since the permeability of a plane channel is known to vary as the third power of the spacing between the two walls, any small variation in this distance may considerably modify the flow. Such variations occur for geological fractures because of the constant modifications of stresses and strains in the underground medium.

Some analytical approaches of this problem can be found in the literature. The elastic deformation of a rough surface in contact with a perfectly flat elastic surface was analyzed by Greenwood and Williamson [1] by using an asperity model; they used the Hertzian contact theory and assumptions about the radius of curvature and heights of asperities and found a relationship between the normal stress and the deformation between a reference surface and the plane of contact. A ''bed of nails'' model for the fracture asperities was developed by Gangi [2] to study the permeability variation of a fracture with the normal load. Tsang and Witherspoon [3] considered the closure of a fracture as the result of the deformation of voids located between the asperities; the behavior of the fracture under a normal stress and the flow variation through it were obtained. Walsh and Grosenbaugh [4] analyzed the stiffness of joints considering the deformations of the asperities and of the surrounding matrix.

The asperity model was generalized by Brown and Scholz [5] by including the composite topography of the fracture surfaces in the joint closure analysis. Theory agreed quantitatively with experiments on ground glass surfaces. Brown and Scholz [6] demonstrated later that the theory can be successfully applied to mated surfaces of fractures if the spatial cross correlations of the surfaces are taken into account. Such a description of fracture surfaces was also applied to the determination of permeability by solving the Reynolds equation [7].

The successful application of the asperity model requires various surface geometry measurements that necessarily involve some uncertainties. Joints with inhomogeneous surfaces or with loose material do not follow the theoretical predictions [5]. Moreover, fractures with correlated surfaces require measurements of the correlation distance.

Surprisingly, in view of the complexity of the problem, there are few numerical models. A joint deformation model was developed by Hopkins *et al.* [8] in order to analyze the relationship between the normal joint stiffness and the spatial geometry of the joint. The joint deformation was supposed to be a combination of the deformation of the half spaces around it and the compression of the asperities separating joint surfaces. The asperities were modeled as disks undergoing an elastic compression. The effect of the contact geometry on the joint stiffness was studied by using a model with asperities of equal height regularly distributed over the fracture plane.

Unger and Mase [9] performed a numerical study of the hydromechanical behavior of fractures with rough self-affine surfaces. Each surface was represented as a series of asperities resting upon a solid half space. During closure, asperities that come into contact undergo compression as one-dimensional rectangular columns and punch into the supporting solid half space. The deformation of the asperities and of the half spaces is determined at a given closure V; the mean contact stress P_c over the contact zone is subsequently deduced.

Some additional references about experimental results on closure of a single fracture subjected to normal load are discussed in Secs. V and VI, which compare the numerical computations and the experimental data.

This paper is organised as follows. Section II is devoted to a general presentation of the problem. Basically, a fracture separates two semi-infinite solid blocks on which a uniform load is applied at infinity. Because of this load, the fracture undergoes some deformation that tends to reduce the fracture permeability. The resolution of this problem necessitates several ingredients. The solid matrix is assumed to be an

*Permanent address: Institute for Problems in Mechanics, Russian Academy of Sciences, 101 prosp. Vernadskogo, Moscow 117526, Russia.

elastic solid and the local displacements are obtained by solving the basic equations of elastostatics. The flow through the fracture is derived from the Stokes equations; the permeabilities of the initial and of the deformed fractures are easily obtained by calculating the average flow rate.

Three types of fractures are addressed in this paper. A simple deterministic case is studied for comparison purposes. Two random fractures are generated with a Gaussian distribution of the surface heights; these heights are correlated in the fracture plane either by a Gaussian or by a self-affine correlation.

Section III is devoted to a mean field analysis of the deformation of the fracture surfaces. The basic element of this analysis is a classical lubrication-type formula (cf. Landau and Lifshitz [10]), which gives the deformation of a solid half space when the distribution of the surface stresses is known. A mean field approximation of the stress distribution enables the calculation of the fracture closure and of the normal joint stiffness in the linear and the nonlinear regimes.

Since realistic stochastic models of fractures are employed and no approximation is used in the calculation of deformations and flow, numerical tools are necessarily employed. All the relevant details and the range of parameters studied are given in Sec. IV. Such a direct treatment of this physical situation has never been done to the best of our knowledge.

Section V presents the variations of fracture closure with applied normal load P. The evolution of the local fracture aperture b with the load P is for a Gaussian fracture; it is shown that the deformation field is almost uniform for small contact areas S_c. Then, the variation of the mean aperture with P is presented; the new contacts are shown to significantly influence the evolution of the aperture. The normal stiffness is analyzed as a function of the fractional contact area S_c. A satisfactory agreement with the predictions of the mean field theory and available experimental data is obtained.

The variations of the fracture permeability with normal stress are discussed in Sec. VI. The dependence of the hydraulic aperture upon P is similar to the mechanical properties. The hydraulic and mean aperture data approximately verify a linear relation. The comparison with experimental data is satisfactory. Some concluding remarks end this paper.

II. GENERAL

A. General description

Consider two semi-infinite pieces of rocks that are partially in contact on an almost plane surface; this situation is depicted in Fig. 1; the fracture is the void volume between the two solid half spaces. A fluid is flowing through the fracture. Suppose now that external forces are exerted on these two rocks in order to produce a uniform pressure P at an infinite distance of the fracture. The two rocks are modeled as perfectly elastic solids. Because of this external pressure, they will undergo deformation and the shape of the fracture will be modified. The new geometry of the fracture will influence the flow and subsequently the permeability of the fracture.

The two surfaces of a fracture are described by the heights $z=h^{\pm}(x,y)$ above an arbitrary reference plane $z=0$ (Fig. 1).

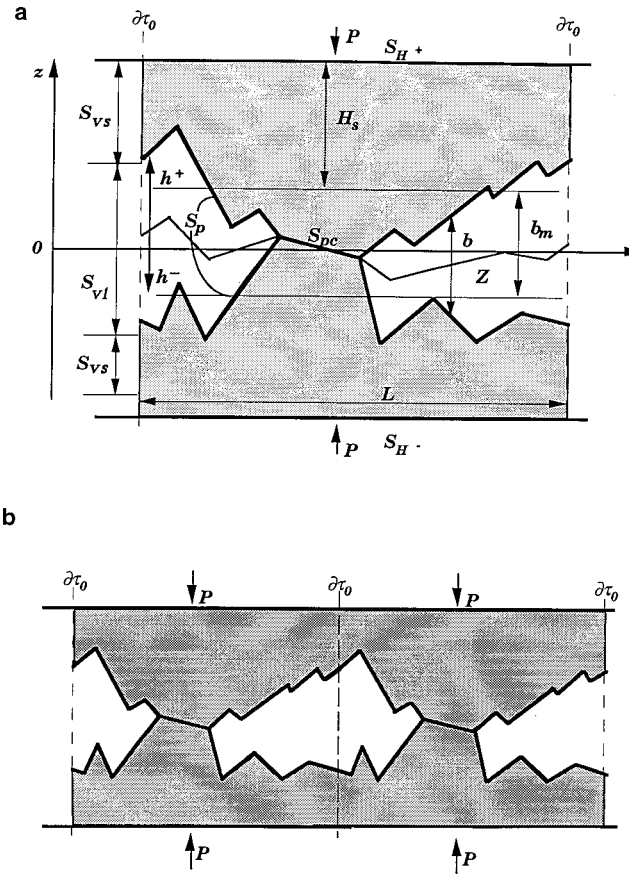

FIG. 1. Conventions and notations for the fracture geometry. Only one unit cell is displayed in (a) and two in (b).

The aperture b of a fracture is the difference between h^+ and h^- when it is non-negative

$$b=\begin{cases} w, & w\geq 0 \\ 0, & w<0, \end{cases} \tag{1}$$

$$w=h^+-h^-.$$

When w is negative, the surfaces are considered to be in contact and $h^+=h^-=0$.

The closure of a fracture under normal load can be defined in the following way. In experimental studies, a uniform normal load is exerted on a fractured sample, and local displacements are measured. In order to reduce effects of nonuniform loading, the averages of several strain gauge outputs are taken. The mean closure of a fracture is directly measured by linear variable displacement transducers (LVDT), which are located close to the fracture [11] or computed by subtracting the deformation of the solid sample from the deformation of the part of the sample containing the fracture [6]. Then, the closure of a fracture is defined as the mean difference between the displacements of each fracture surface

$$V=\langle \Delta h^+-\Delta h^- \rangle. \tag{2}$$

It can be shown from Eqs. (1) and (2) that the closure V may be expressed as

$$V=\langle b_{\text{in}} \rangle-\langle b \rangle, \tag{3}$$

where b_{in} is the initial aperture of the fracture. The average value $\langle b \rangle$ is calculated over the total area of the fracture projection.

This definition is used in the present work though other definitions are possible (cf., for instance, Unger and Mase [9]). A uniform normal load P (i.e., a force per unit surface) is applied at an infinite distance of the fracture to both solid half spaces. The total displacements **d** are calculated for each value of P by solving the elastostatic equations; it is important to notice that the local stresses are neither uniform, nor normal close to the fracture surface. The closure V is deduced from Eq. (3), and the geometrical evolution of the void volume is characterized.

Once the deformation of the fracture is determined as a function of the load P, the permeability of the fracture has to be estimated. The hydraulic properties of the fractures are characterized by the Stokes permeability $\mathbf{B}_S$ and the hydraulic aperture of the fracture b_S. The Stokes permeability tensor $\mathbf{B}_S$ is defined by the equation

$$\overline{\mathbf{Q}_S} = -\frac{1}{\mu}\,\mathbf{B}_S \cdot \overline{\nabla p}, \tag{4}$$

where $\overline{\mathbf{Q}_S}$ is the mean flow rate per unit fracture width, μ the fluid viscosity, and $\overline{\nabla p}$ the macroscopic pressure gradient. When the fracture is isotropic, $\mathbf{B}_S$ reduces to $B_S\mathbf{I}$ where $\mathbf{I}$ is the two-dimensional unit tensor. The permeability $\mathbf{B}_S$ is derived from the solution of the Stokes equations, which are described in Sec. II C. For isotropic fractures, the hydraulic aperture b_S is defined as

$$b_S = (12B_S)^{1/3}. \tag{5}$$

In real fractures that contain an incompressible fluid, the deformation of the matrix may be considered as the result of the equilibrium between the applied normal stresses and the fluid pressure acting on the fracture surfaces. In most cases, the variations of the fluid pressure along the fracture plane are negligible compared to the mean pressure acting on the surfaces. Hence, the deformations can be calculated for the effective normal load, which is the difference between the real applied load and the mean fluid pressure in the fracture. Therefore, the mechanical and hydraulic behaviors of the fracture are considered separately; this means that the solid matrix displacements under the applied load P are calculated without taking into account the fluid pressure in the fracture.

Thus, the stress strain behavior of a fracture embedded in an elastic solid matrix is studied in terms of the applied normal load P and of the fracture closure V.

Before this general presentation is concluded, the following limitation should be emphasized. The deformations of the solid matrix are determined by the linear elasticity theory where only small deformations **d** can be studied. When P increases, **d** increases linearly. For some critical value P_c, opposite surfaces of the fracture eventually touch each other and some new contact zone appears. This new contact should be taken into account in the calculation of the displacement field for $P > P_c$; hence, the initial fracture geometry should be modified and a new displacement field calculated.

The general equations that govern the physical situation depicted in Fig. 1 will be presented in the rest of this section. As a general rule, in the numerical calculations, the space is replaced by a three-dimensional unit cell centered around the mean fracture plane; spatially periodic boundary conditions are imposed on the two lateral boundaries parallel to the x-z and y-z planes and denoted by $\partial\tau_0$ in Fig. 1.

For the sake of clarity, the numerical method of solution is postponed to Sec. IV.

B. Deformation model

The solid matrix in which the fracture is embedded is supposed to be perfectly elastic. The equations that govern the elastic behavior of the material are the basic equations of elastostatics. Let $\boldsymbol{\sigma}$ denote the stress tensor; in the absence of any external volumetric force, the equilibrium equation reads as

$$\boldsymbol{\nabla} \cdot \boldsymbol{\sigma} = \mathbf{0}. \tag{6a}$$

The strain tensor **e** is expressed in terms of the displacement **d**,

$$\mathbf{e} = [\nabla \mathbf{d} + (\nabla \mathbf{d})^t]/2, \tag{6b}$$

where the superscript t denotes the transposition operator. Only isotropic solid matrices are considered here. Hence, the stress tensor is given by

$$\boldsymbol{\sigma} = l\ \mathrm{tr}\mathbf{e} \cdot \mathbf{I} + 2m\mathbf{e}, \tag{6c}$$

where l and m are the familiar Lamé coefficients. For future use, the Young modulus $E = (3l + 2m)m/(l + m)$ and the Poisson ratio $\nu = l/2(l + m)$ can be defined.

These equations have to be supplemented with boundary conditions at the free fracture surfaces S_p. Let us simply assume that no external force is exerted at this interface whose unit normal is **n**:

$$\boldsymbol{\sigma} \cdot \mathbf{n} = 0 \quad \text{on} \quad S_p. \tag{6d}$$

Equivalently, the equilibrium equation can be expressed in terms of the displacement **d**,

$$(l + m)\nabla(\boldsymbol{\nabla} \cdot \mathbf{d}) + m\nabla^2 \mathbf{d} = 0 \tag{7a}$$

together with the condition of no stress at the boundary S_p of the solid phase

$$\{m[\nabla \mathbf{d} + (\nabla \mathbf{d})^t] + l(\boldsymbol{\nabla} \cdot \mathbf{d})\mathbf{I}\} \cdot \mathbf{n} = 0, \quad \boldsymbol{\sigma} \cdot \mathbf{n} = \mathbf{0} \quad \text{on} \quad S_p. \tag{7b}$$

Periodic conditions are applied on the vertical boundaries $\partial\tau_0$ of the unit cell of the periodic system. Far from the fracture plane, a uniform fixed normal load P is applied:

$$\sigma_{zz} = -P, \quad z \to \pm\infty. \tag{8}$$

When the fracture surfaces touch one another, they are assumed to be cemented and the stress and strain are continuous at the contact surface S_{pc}:

$$\boldsymbol{\sigma}^+ = \boldsymbol{\sigma}^-, \quad \mathbf{d}^+ = \mathbf{d}^- \quad \text{on} \quad S_{pc} \tag{9}$$

When the elastic problem is solved, the mean aperture $\langle b \rangle$ and the fracture closure V are easily calculated as functions of the normal load P. The normal joint stiffness can be defined as [12]

$$k = \frac{dP}{dV}. \tag{10}$$

The normal joint stiffness is widely used to describe the behavior of fractures under load and can be measured in the laboratory [13–15].

C. Fluid flow model

For each value of the load P, the geometry of the fracture void volume can be determined and the mean permeability B_S calculated by numerically solving the Navier-Stokes equations in the low Reynolds number limit as done by Mourzenko *et al.* [16].

The analysis of Stokes flow is very similar to that made for three-dimensional porous media (cf. Adler [17]). Consider an infinite fracture made of identical unit cells of size $L \times L$ in the x-y plane. The low Reynolds number flow of an incompressible Newtonian fluid through a fracture is governed by the usual three-dimensional (3D) Stokes equations

$$\nabla p = \mu \nabla^2 \mathbf{v}, \quad \boldsymbol{\nabla} \cdot \mathbf{v} = \mathbf{0}, \tag{11}$$

where $\mathbf{v}$, p, and μ are the velocity, pressure, and viscosity of the fluid, respectively. In general, $\mathbf{v}$ satisfies the conditions

$$\mathbf{v} = \mathbf{0} \quad \text{on the total surface } S \text{ of the fracture} \tag{12a}$$

and

$$\mathbf{v} \quad \text{is spatially periodic with period } L \text{ in the plane of the fracture} \tag{12b}$$

This system of equations and conditions applies locally at each point $\boldsymbol{r}$ of the interstitial fluid. In addition, it is assumed that the macroscopic pressure gradient $\overline{\nabla p}$ is specified;

$$\overline{\nabla p} = \frac{1}{\tau_l} \int_{\partial \tau_0} p \, d\mathbf{s} = (\text{a prescribed constant vector}), \tag{13}$$

where τ_l is the volume of the fracture; τ_l is bounded by the two solid surfaces S_p and the vertical boundary of the fraction S_{vl} of the unit cell in the fracture volume, so that $\partial \tau_l = S_{vl} \cup S_p$ (see Fig. 1). The mean flow rate $\overline{\mathbf{Q}_S}$ per unit fracture width may be defined as

$$\overline{\mathbf{Q}_S} = \frac{1}{S^*} \int_{\tau_l} \mathbf{v} \, d^3\mathbf{r}, \tag{14}$$

where S^* is the area of the x-y projection of S_p and S_{pc}. $\overline{\mathbf{Q}_S}$ is linearly related to the pressure gradient $\overline{\nabla p}$ by the Stokes permeability tensor $\mathbf{B}_S$ by the classical relation (4). Further details on some technical points such as the spatially periodic boundary conditions can be found in Ref. [17].

D. Description of fractures

The two surfaces of the fracture are described by the heights $z = h^{\pm}(x,y)$ above an arbitrary reference plane $z = 0$ (Fig. 1). Usually, $h^{\pm}$ are random functions; they can be characterized by the two probability densities $\varphi(Z)$ and $\varphi(w)$ of the mean surface $Z = (h^+ + h^-)/2$ and of the distance $w = h^+ - h^-$, which are often assumed to be Gaussian,

$$\varphi(F) = \frac{1}{\sqrt{2\pi\sigma_F}} \exp\left(- \frac{(F - \langle F \rangle)^2}{2\sigma_F^2} \right), \quad F = Z, w, h, \tag{15}$$

where σ_F^2 denotes the variance $\langle (F - \langle F \rangle)^2 \rangle$; the angular brackets correspond to the statistical average. For instance, σ_h denotes the root-mean-square roughness of the surface.

The aperture b of the fracture is defined by Eq. (1) and may be described by its mean $\langle b \rangle$ and its variance σ_b^2, which are generally not equal to the mean separation $b_m = \langle w \rangle$ and to σ_w^2, respectively; of course, the differences between these values is due to the partial overlap of the fractures (cf. Mourzenko *et al.* [18]). When w is negative, the surfaces are considered to be in contact and one has $h^+ = h^- = Z$.

A series of fractures is obtained with the same fields $h^{\pm}$, but different b_m. For some values of b_m, the initial separation w becomes negative and such zones correspond to initial contacts between the two fracture surfaces. In the initial state, which is characterized by $h^{\pm}$ and b_m, the fracture is considered to be in equilibrium. The deformation of the solid matrices is described by the increments $\delta h^{\pm}$.

The statistical properties of the fracture in the x-y plane can be characterized by the spatial correlations of the fields h^+ and h^-, which are described by the covariance functions $C_Z(r)$ and $C_w(r)$:

$$C_F(r) = \langle \{F(x,y) - \langle F \rangle\} \{F(x + \Delta x, y + \Delta y) - \langle F \rangle\} \rangle, \quad r = \sqrt{\Delta x^2 + \Delta y^2}, \quad F = Z, w. \tag{16}$$

Two types of random fractures will be addressed in this paper, namely, Gaussian and self-affine fractures. For the so-called Gaussian fractures, all the quantities h^+, h^-, Z, and w were described by the quadratic covariance function

$$C_F(r) = \sigma_F^2 \exp\left[- \left(\frac{r}{l_F} \right)^2 \right], \tag{17}$$

where l_F is the correlation length of the field F.

Self-affine fractures were also used since there exist many experimental observations where the self-affine character of rock surfaces is demonstrated [5]. Self-affine surfaces have features over a broad range of characteristic length scales and can be described by the covariance

$$C_h(r)=\sigma_h^2\left[1-\left(\frac{r}{l}\right)^{2\zeta}\right], \tag{18}$$

where l is a characteristic length and ζ is the roughness exponent that was found to be 0.87 ± 0.07 [19,20].

Finally, the upper and lower surfaces can be either correlated or not correlated. The correlation between the two surfaces is characterized by the correlation parameter $\theta=1-\sigma_w^2/2\sigma_h^2$, which is 0 for uncorrelated surfaces and 1 for fully correlated surfaces. Hence, all the possible situations can be described by the nature of the correlation in the x-y plane and by the three parameters b_m/σ_h, l/σ_h, and θ; this is equivalent to considering σ_h as the length unit.

III. A MEAN FIELD ANALYSIS

In order to perform a first application of the set of equations that govern the phenomenon and provide a theoretical basis for the analysis of the numerical results relative to fracture compression, a simple deformation model has been developed.

Recall that in the initial state ($P=0$), the solid may be already strained, since a stress field and a displacement field with respect to a rest state where the fracture surfaces are totally separated may exist. In such a case, the solid is assumed to be everywhere in its elastic domain and the linear elasticity theory applies. Therefore, these initial stresses and strains may be ignored, and the additional displacement **d** resulting from an additional normal load P is determined from Eqs. (7)–(9).

The following derivation approximates the three-dimensional character of the problem at hand by using a lubrication approximation. Basically, the deformation of the fracture surfaces with respect to their initial profile is evaluated by assuming that the initial fracture surfaces are almost plane and remain so under the load P, and that the surface displacements δh are normal to this plane. This leads to a mixed boundary value problem, where zero stress is imposed on the open zones of the fracture surface and zero displacement is imposed in the contact zones (assuming that the fracture is symmetric). The normal stress P_{cs} in the contact surface is not uniform and must satisfy the overall equilibrium condition [Fig. 2(a)]:

$$\int_{\Sigma_c}\int P_{cs}(\mathbf{r})d^2\mathbf{r}=\Sigma_T P, \tag{19a}$$

where Σ_T and Σ_c are the total area of the fracture and the area of the contact zone, respectively.

This problem will be simplified further by assuming that P_{cs} is uniform over Σ_c; it should be noticed that this assumption is only a mean field approximation, which is the simplest possible estimate of P_{cs}; it does not mean that the deformation is plastic over the contact zone. The condition (19.a) yields

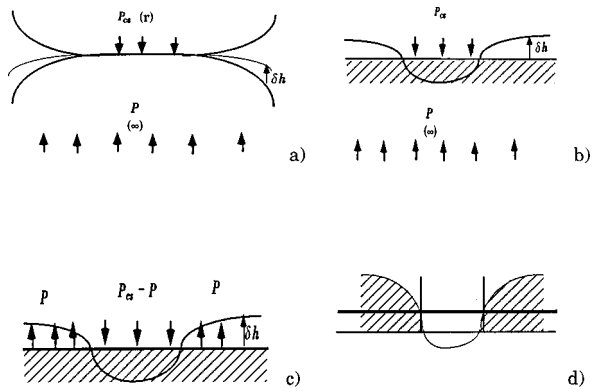

FIG. 2. Mean field analysis of the deformation of the fracture surfaces under a load P: (a) distribution of the normal stress P_c in the contact surface; (b) reduction of the mixed boundary value problem to a Neumann problem; (c) shift of the stress conditions; (d) evaluation of the new position of the contact surface.

$$P_{cs}=\frac{\Sigma_T}{\Sigma_c}P. \tag{19b}$$

The problem reduces to a Neumann problem (in terms of the displacements), with a stepwise distribution of stresses on the fracture surfaces 0 and P_{cs} in the noncontact and contact zones, respectively [Fig. 2(b)]. Obviously, this approximation is only valid for $\Sigma_c \ll \Sigma_T$. If the contact zones are very small, the normal stresses on Σ_c act as point forces on the fracture surfaces, and their exact distribution has little influence.

Finally, note that the deformation of a fracture surface can be evaluated by shifting the stress conditions on the surface and at infinity by $-P$. Each solid block is viewed as a semi-infinite half space, undergoing a pressure $P_{cs}-P$ in Σ_c and a tension P in $\Sigma_T-\Sigma_c$ [Fig. 2(c)]. Since the overall position of the fracture surface has been allowed to drift when the zero-displacement condition was replaced by a stress condition on Σ_c, the deformation of the surface has to be taken relative to the new position $\overline{\delta h_c}$ of the contact zones in order to evaluate the closure of the fracture [Fig. 2(d)], which is given by

$$\begin{aligned}V&=\frac{2}{\Sigma_T}\iint_{\Sigma_T}[\delta h(\mathbf{r})-\overline{\delta h_c}]d^2\mathbf{r}\\&=\frac{2}{\Sigma_T}\iint_{\Sigma_T-\Sigma_c}[\delta h(\mathbf{r})-\overline{\delta h_c}]d^2\mathbf{r}.\end{aligned} \tag{20}$$

The factor 2 corresponds to the contributions of both surfaces to the closure. Since δh is not uniform on Σ_c, $\overline{\delta h_c}$ is defined as its average:

$$\overline{\delta h_c}=\frac{1}{\Sigma_c}\iint_{\Sigma_c}\delta h(\mathbf{r})d^2\mathbf{r}. \tag{21}$$

The displacement of the surface δh can be easily calculated by the surface integral [10]

$$\delta h(\mathbf{x})=\frac{1-\nu^2}{\pi E}\iint_{\Sigma_T}\frac{P(\mathbf{r})d^2\mathbf{r}}{|\mathbf{r}-\mathbf{x}|}. \tag{22}$$

Equivalently, with Eq. (19b),

$$\delta h(\mathbf{x}) = \frac{1-\nu^2}{\pi E} P\left\{ \iint_{\Sigma_T-\Sigma_c} \frac{d^2\mathbf{r}}{|\mathbf{r}-\mathbf{x}|} - \frac{\Sigma_T-\Sigma_c}{\Sigma_c} \iint_{\Sigma_c} \frac{d^2\mathbf{r}}{|\mathbf{r}-\mathbf{x}|} \right\}, \tag{23}$$

where ν is the Poisson ratio and E the Young modulus.

We introduce the contact function $\Sigma_c(\mathbf{r})$:

$$Z_c(\mathbf{r}) = \begin{cases} 1, & \mathbf{r} \in \Sigma_c \\ 0, & \mathbf{r} \notin \Sigma_c \end{cases}. \tag{24}$$

Using Eqs. (24), (19b), and (22) $\delta h(\mathbf{x})$ can be written as

$$\delta h(\mathbf{x}) = \frac{1-\nu^2}{\pi E} P \frac{1}{S_c} \iint_{\Sigma_T} (\overline{Z_c} - Z_c) \frac{d^2\mathbf{r}}{|\mathbf{r}-\mathbf{x}|},$$

$$\overline{Z_c} = \frac{1}{\Sigma_T} \iint_{\Sigma_T} Z_c \, d^2\mathbf{r}, \tag{25}$$

where $S_c = \overline{Z_c}$ is the fractional contact area, since it represents the fraction of the total area Σ_T of the fracture corresponding to the contact area. This expression can be used in the expression (20) of the closure; if $\Sigma_c(\mathbf{r})$ is a random stationary isotropic field and if Σ_T is large enough that the ergodicity hypothesis can be used, the surface integrals can be expressed in terms of the correlation length $\mathcal{L}$ of the normalized covariance $R_c(t)$ of the random field $\Sigma_c(\mathbf{r})$:

$$\mathcal{L} = \int_0^{+\infty} R_c(t) dt. \tag{26}$$

If $\mathcal{L}$ is finite, which is generally true for random fractures without long-range order, the closure is obtained as

$$V = \frac{4(1-\nu^2)}{E} \frac{1-S_c}{S_c} P\mathcal{L}. \tag{27}$$

The normal joint stiffness k defined by Eq. (10) can be subsequently expressed as

$$k = \frac{E}{4(1-\nu^2)\mathcal{L}} \frac{S_c}{1-S_c}. \tag{28}$$

In the case of fracture surfaces with normally distributed random heights, the fractional contact area S_c and the correlation length $\mathcal{L}$ can be determined when b_m/σ_h and the covariance $C_w(t)$ are known. The stiffness k is evaluated in the Appendix for fractures with Gaussian and self-affine correlations [Eqs. (A9) and (A10)]. Limiting expressions for $b_m/\sigma_h \to 0$ or ∞ are also provided in the Appendix.

This analysis can be tentatively extended to the nonlinear domain where new contact zones appear. Such a phenomenon occurs at the border of the initial contact; if the two fractures are tangent, this phenomenon occurs immediately as in the classical Herz theory between two spheres [10]. The relation (27) can be differentiated with respect to P with the help of Eq. (3) to yield

$$\frac{dP}{d\langle b \rangle} = -\frac{E}{4(1-\nu^2)\mathcal{L}} \frac{S_c}{1-S_c} = -k. \tag{29}$$

Suppose that the heights remain normally distributed with the same σ_h. Because of ergodicity, the mean aperture $\langle b \rangle$ and the fractional contact area S_c are related to the mean separation b_m by

$$S_c = \frac{1}{2}\left\{ 1 - \mathrm{erf}\left(\frac{b_m}{2\sigma_h} \right) \right\}, \tag{30}$$

$$\langle b \rangle = (1-S_c) b_m + \frac{\sigma_h}{\sqrt{\pi}} \exp\left(-\frac{b_m^2}{4\sigma_h^2} \right), \tag{31}$$

where erf denotes the classical error function. Introduction of Eqs. (30), (31), and (A9) into Eq. (29) yields

$$\frac{dP}{db_m} = -\frac{E}{4(1-\nu^2) l} \frac{S_c^2}{\Psi_\tau(S_c)(1-S_c)}, \quad \tau = G, s, \tag{32}$$

where Ψ_τ is defined by Eq. (A10).

The closed system (30) and (32) is the basis of a nonlinear analysis of the fracture closure for small S_c. A full description of the hydromechanical behavior of fractures requires a relation between $b_S = (12 B_S)^{1/3}$ and the geometrical parameters b_m/σ_h and l/σ_h. The numerical results of Mourzenko *et al.* [16] can provide such a dependence. Moreover, the system (30), (32) and the formulas (3), (28), (31) provide a stress-closure relation and the dependence of the stiffness k upon P.

Figure 3 shows the results obtained by using the nonlinear theory (28), (30), (32) for Gaussian and self-affine fractures. The stress-closure curves are presented in Fig. 3(a). One can see that the deformation history of the fractures is influenced by the spatial correlations of surface profiles.

The normal load P is a decreasing function of the aperture b_m/σ_h. However, with the Gaussian fracture surface height distribution (15), $P=0$ is obtained only for infinite aperture, since contact zones remain for any finite value of b_m. The decay rate of P in a real fracture depends on the tail of the height distribution function, which may be inaccurately represented by a Gaussian distribution. This illustrates the difficulty to define a hypothetical rest state for a prestrained fracture.

Therefore, a stiffness-to-contact area or stiffness-to-normal load relationship might be preferred for comparison purposes to the load-to-aperture one. Figure 3(b) shows the dimensionless stiffness $k\sigma_h/E$ as a function of the normal load P/E. Quasilinear relations are obtained for $P/E > 10^{-3}$, i.e., for moderate apertures $b_m/\sigma_h \leqslant 3.5$–$4$. This character agrees with the results for uncorrelated fractures [14,20]. Further comparisons with experimental data will be commented on in Sec. V D.

IV. GEOMETRIC PARAMETERS AND NUMERICAL METHODOLOGY

This section provides the major numerical ingredients necessary to calculate the deformations of a fracture submitted to a normal load and the resulting permeability changes. Computations will be performed on a finite volume, which is

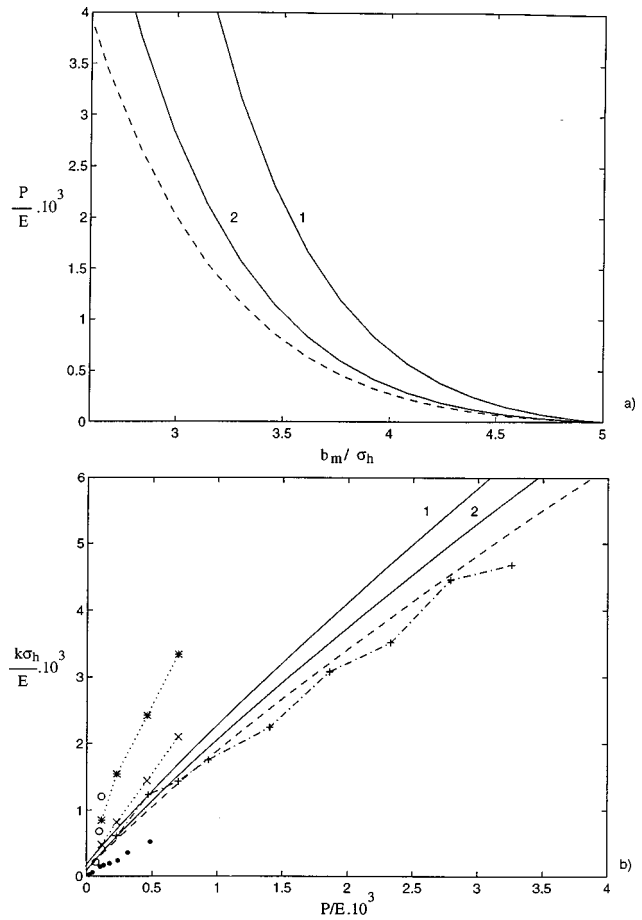

FIG. 3. (a) Variations of the normal load P/E as a function of b_m/σ_h during a fracture closure as predicted by the mean field theory. Data are for Gaussian fractures (solid lines) with $l/\sigma_h=1$ and 2 and for a self-affine fracture (dashed line) with $\zeta=0.5$, $l/\sigma_h=6$. (b) The dimensionless fracture stiffness $k\sigma_h/E$ as a function of P/E. The dotted lines are Yoshioka and Scholz's [26] measurements for ''rough'' (∗) and ''smooth'' (×) surfaces. The dash-dotted line corresponds to the data of Durham and Bonner [27]. The open circles are the data of Boitnott and Scholz [31] for ground optical glass and the solid circles are the measurements of Engelder and Scholz [30] in Cheshire quarzite.

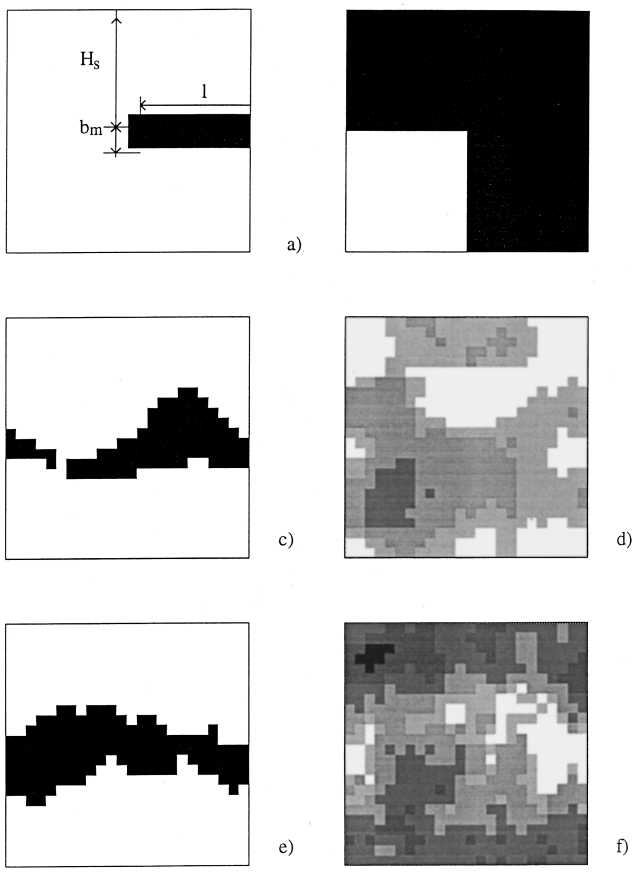

FIG. 4. The simulated fracture profiles [(a), (c), and (e)] and aperture distributions [(b), (d) and (f)] for the three fracture geometry models. Six levels of shadings are distinguished from zero (white) to the largest value (dark) of the aperture. The shading steps are equal to $0.8\sigma_h$. Data are for $H_s=1.25l$, $b_m/\sigma_h=3.46$ for the step fracture (a), (b), $H_s=1.82l$, $b_m/\sigma_h=0.5$, $l/\sigma_h=2$ for the Gaussian fracture (c), (d), and $H_s=0.92l$, $b_m/\sigma_h=1$, $l/\sigma_h=6$, $\zeta=0.5$ (e),(f) for the self-affine fracture.

discretized into $N_c\times N_c\times N_{cz}$ elementary cubes of size a [cf. Fig. 5(a)], spatially periodic boundary conditions are generally used in the x-y plane. The elementary cubes are either solid or liquid. The mesh spacing inside these cubes is a fraction $1/n$ of a; it is the same in all three directions, but may be different in the liquid and the solid phases.

A. Geometric parameters of the initial fractures

A first simple deterministic model (hereafter referred to as M), which is called the step fracture model [Figs. 4(a) and 4(b)] is used in order to study the elastic compression of two regular surfaces that are initially in contact with $S_c=0.25$. The asperity is a parallelepipedon of height a, with a square basis of side $l=5a$; the size of the unit cell is $L=10a$. This yields equivalent average ratios $b_m/\sigma_h=2\sqrt{3}$ and $\sigma_h/a=\sqrt{3}/4$. The ratio of horizontal and vertical asperity scales [cf. Fig. 4(a)] $l/\sigma_h=20/\sqrt{3}\approx 12$. Three samples with various heights H_s were studied (see Table I) in order to analyze the influence of this parameter.

The random fields Z and w for the Gaussian and self-affine fractures are generated by the method of Fourier transforms (see Ref. [17] for details) on the $N_c\times N_c$ numerical grid in the x-y plane with elementary surfaces of size a.

As a matter of fact, only uncorrelated surfaces with $\theta=0$ were addressed in this work for the sake of simplicity. However, this is not a limitation inherent to our methodology and correlated surfaces can be dealt with. Note that the length $N_c a$ is much larger than any correlation or characteristic length of the fracture surfaces.

Four Gaussian fractures were obtained with the same random surfaces, but various separations b_m. The correlation distance l/σ_h was set equal to 2, and the sample size $L/l\approx 4$ in order to minimize statistical errors (see Fig. 4). The mean separation b_m/σ_h varies between 0.25 and 1; therefore, the fractional contact area S_c varies between 0.444 and 0.125 (see Table I). Each fracture is denoted by G_{b_m}/σ_h. These values of S_c were found in various experiments of fracture compression [3,14,22].

Three self-affine fractures were generated with $\zeta=0.5$ and $b_m/\sigma_h=0.5$, 1, and 1.5 (cf. Fig. 4). Again they are denoted by S_{b_m}/σ_h. Because spatially periodic fractures are gener-

TABLE I. Geometrical parameters of fractures. l is equal to the horizontal size of the asperity for the step fracture model and to half the size of the sample for the self-affine fractures. The index for G and S stands for the value of b_m/σ_h.

Sample name	$\frac{\sigma_h}{a}$	$\frac{l}{\sigma_h}$	$\frac{b_m}{\sigma_h}$	$\frac{L}{\sigma_h}$	$\frac{\langle b\rangle}{\sigma_h}$	S_c	$\frac{H_s}{l}$
			Step fracture model				
M_6	0.433	11.6	3.46	22.6	3.46	0.25	0.45
M_{10}	0.433	11.6	3.46	22.6	3.46	0.25	0.85
M_{14}	0.433	11.6	3.46	22.6	3.46	0.25	1.25
			Gaussian fractures				
$G_{1/4}$	3.03	2	0.25	7.92	0.472	0.444	1.86
$G_{1/2}$	3.03	2	0.5	7.92	0.649	0.311	1.82
$G_{3/4}$	3.03	2	0.75	7.92	0.858	0.196	1.77
G_1	3.03	2	1.0	7.92	1.075	0.125	1.71
			Self-affine fractures				
$S_{1/2}$	2	6	0.5	12	0.951	0.315	0.96
S_1	2	6	1.0	12	1.359	0.180	0.92
$S_{3/2}$	2	6	1.5	12	1.805	0.100	0.88

ated, the covariance (18) describes the surface height correlations only for distances smaller than $L/2$ and the characteristic length l in Eq. (18) is chosen to be equal to $L/2$. The corresponding geometric parameters are presented in Table I.

Further details on the generation of random fractures can be found in Mourzenko *et al.* [18].

B. Computations of deformations

Deformations are obtained by solving the system of equations (6), (8), (9). However, it should be noticed that the overall conditions (8) cannot be perfectly achieved neither in real experiments nor in numerical models and should be replaced by approximate conditions on two planes located at some distance H_s from the mean plane of the fracture surfaces (see Fig. 1):

$$\sigma_{zz} = -P \quad \text{on} \quad S_H^{\pm}. \tag{33}$$

The system of equations (6), (8), (9) is solved via a second-order finite difference formulation. It is first discretized by means of the finite volume method in terms of the unknown displacements **d**. Details are given in Ref. [23]. It should be noticed that each elementary cube a is subdivided into n^3 elements where n is at least equal to 3, so that the order of the method is equal to two. The resulting linear system is solved by using a conjugate gradient method with a precision Δ_r of the order of 10^{-2}.

Once the field **d** is determined, the new position $h^{\pm} + \delta h^{\pm}$ of the fracture surfaces can be derived. Consider an elementary solid cube C_1 of size a/n whose face ΔS belongs to the fracture surface [Fig. 5(a)]. The normal displacement δh of ΔS is equal to

$$\delta h = \mathbf{n}\cdot\mathbf{d}_S = \mathbf{n}\cdot\left(\mathbf{d} + \frac{a}{2n}\,\mathbf{n}\cdot\nabla\mathbf{d}\right), \tag{34}$$

where **n** is the unit normal of ΔS oriented from C_1 to the neighboring void cube C_2, $\mathbf{d}_S$ the displacement of ΔS. Equation (34) provides the values δh of the local normal displacements which linearly depend upon the normal load P. In order to obtain a discrete representation of the modified geometry of the fracture space, the following algorithm is proposed. The solid fraction ε_S in the neighboring elementary liquid cube C_2 because of the displacement of ΔS [Fig. 5(b)] is readily derived from Eq. (34) as

$$\varepsilon_S = \frac{1}{a^3}\iint_{\Delta S}\delta h\, d\sigma = \frac{n}{a}\,\delta h. \tag{35}$$

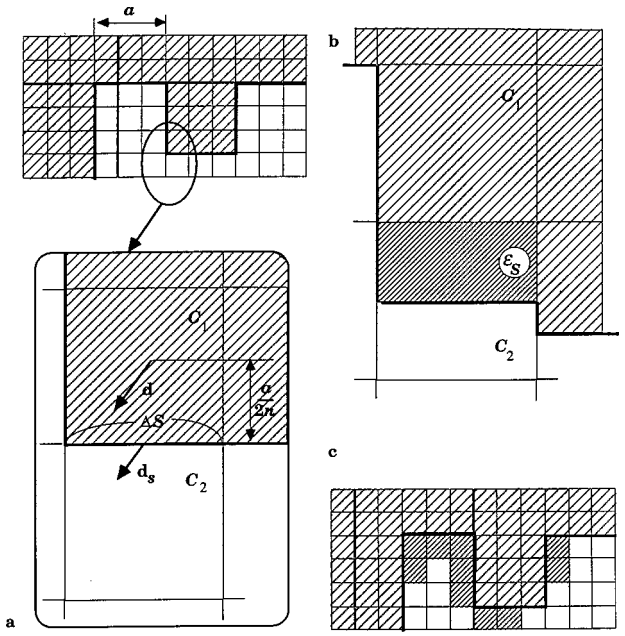

FIG. 5. (a) Position of the fracture surface in the mesh. The size of the elementary cube is a, the fraction factor $n=3$. The solid phase is shadowed. (b) The solid fraction ε_S in the elementary cube C_2 after the displacement of the face ΔS of the fracture surface. (c) Position of the fracture surface in the deformed state. The new solid cubes are denoted by the darkest shadowing.

TABLE II. The standard deviation $\sigma_{d^\pm}$ of the displacements on upper and lower boundaries of the samples.

	M_6	M_{10}	M_{14}	$G_{1/2}$	G_1
H_s/l	0.45	0.85	1.25	1.82	1.71
$\sigma_{d^-}/\langle d_z^- \rangle$	0.462	0.151	0.048	0.122	0.08
$\sigma_{d^+}/\langle d_z^+ \rangle$	0.462	0.151	0.048	0.094	0.128

This procedure can be applied to all the solid faces of C_2. When ε_S is larger than a threshold ε_S^*, which is generally equal to 0.5, the liquid cube is changed into solid and the fracture geometry is modified accordingly. This procedure is performed for all the cubes C_k that possess one face or more on the fracture surface [Fig. 5(c)].

The first limitation of this approximation is the possible appearance of new contact zones. Any change in the contact area is not accounted for by the system (6), (8), (9). Should the two surfaces of the fracture touch each other for some value P_c, the system (6), (8), (9) has to be solved again for this new geometry. Otherwise, the extension of the calculations for $P > P_c$ would implicitly assume that the two surfaces may freely overlap. This point will be taken into account in Sec. V.

The second limitation is due to the boundary condition (8). Displacements on $S_H^\pm$ are not uniform, because of the finite distance from the fracture. In order to estimate the error, the standard deviation $\sigma_d^\pm$ of the displacements on $S_H^\pm$ is calculated as

$$\sigma_d^\pm = \langle (d_z^\pm)^2 - \langle d_z^\pm \rangle^2 \rangle^{1/2}. \tag{36}$$

The angular brackets denote here the average over the fracture projection. H_s can be considered as sufficient when $\sigma_d^\pm/\langle d_z^\pm \rangle$ is small.

The influence of H_s on the results was checked as follows. Table II contains the standard deviation of $\sigma_d^\pm$ of the displacements of S_H^+ and S_H^- calculated by using Eq. (36). The error induced by the finite sample height for the step fracture is a decreasing function of H_s/l. For model M, the residual fluctuation $\sigma_d^\pm/\langle d_z^\pm \rangle$ is 0.15 and 0.05 for $H_s/l = 0.85$ and 1.25, respectively. Random fractures require larger heights. For Gaussian fractures, a residue 0.10 is obtained for $H_s \approx 2l$.

C. Computations of the flow

The Stokes equations (11) are solved by the so-called artificial compressibility method with a multigrid algorithm (cf. Ref. [16]). Convergence was reached when the flow rate was found the same within 1% across the various sections of the medium.

A $72 \times 72 \times 72$ mesh was used for most realizations. The size of the elementary cube a was usually equal to $0.3\sigma_h$ for Gaussian fractures and $0.5\sigma_h$ for self-affine ones, and in the refined mesh the steps were $0.1\sigma_h$ and $0.17\sigma_h$, respectively. This discretization is small enough for a good representation of the vertical variations of the surface profiles.

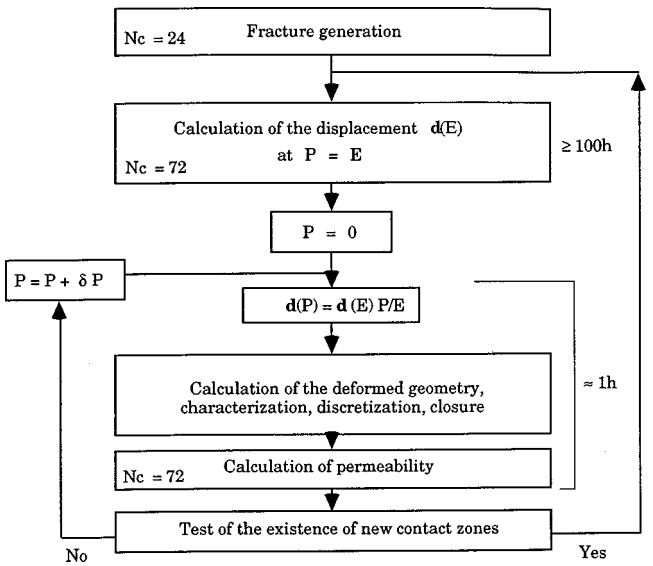

FIG. 6. Scheme of the numerical modeling of the fracture closure under the normal load.

D. Summary of the numerical modeling

It might be useful to the reader to have a summary of the numerical modeling as schematized in Fig. 6.

For each fracture, two random correlated surfaces are generated on a two-dimensional mesh with a step size a. Then, the fracture volume and enclosing solid matrices are subdivided into elementary cubic blocks with the same size a. Then, the displacement vector $\mathbf{d}$ is calculated for an arbitrary load; since a stress has the same dimension as the Young modulus E, P was chosen equal to E. Recall that the order of the method is equal to 2 for $n=3$. On an IBM 560 workstation, this computation lasts for about 100 h, with a memory size of 100 Mbytes for a $72 \times 72 \times 72$ grid.

Thanks to linearity, the deformation $\mathbf{d}(P)$ under any load P can be obtained by

$$\mathbf{d}(P) = P/E \ \mathbf{d}(E). \tag{37}$$

The new geometry of the fracture can be derived from Eq. (34) and various parameters are estimated, such as the mean fracture aperture, the contact area and the permeability. This computation lasts for about 1 h.

The value of P is increased and the calculation of $\mathbf{d}$ is repeated, if new contacts do not appear in the previous step (see Fig. 6). If new contact zones exist for some value P_c, the modified fracture geometry is used as a new initial state for the calculation of a new displacement field $\mathbf{d}(P_c + E)$.

In order to restart the numerical solution of Eq. (7), the modified fracture geometry at P_c has to be rediscretized on the coarser initial mesh with elementary cube size a; otherwise the fine mesh should be divided by $n=3$ again to keep the deformation accurate at the second order. The error induced by this coarsening will be discussed in Sec. V A.

V. RESULTS ON FRACTURE CLOSURE AND NORMAL STIFFNESS

A. Local evolution of the fracture

In order to illustrate the evolution of the fracture aperture b with increasing normal load P/E, the Gaussian fracture G_1 is chosen.

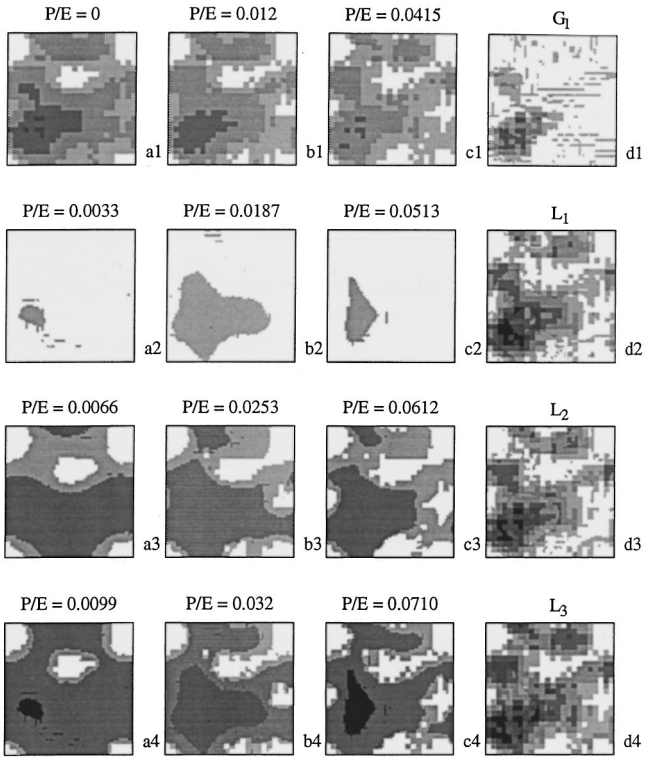

FIG. 7. Aperture distributions. The three columns (a), (b), (c) refer to fractures G_1, L_2, and L_3, respectively. The initial aperture bin is given in Eq. (1) with shading steps equal to $0.9\sigma_h$. The difference $b_{\text{in}}-b$ for three successive loads is given in (2)–(4) with gray levels ranging from white (zero) to black [maximal closure in (4)]. The aperture distributions in G_1, L_1, L_2, L_3 at $P/E=0.071$ are given in the last column (d), with shading steps equal to $0.35\sigma_n$.

Two factors contribute to the increase of the fractional contact area S_c during the fracture closure, namely, the growth of the contact area near the contacting tips of surface asperities, and the appearance of new contacts. The first factor provides an almost continuous increase of S_c with P, which was observed in experiments by Gentier [11]. It is obvious that this behavior cannot be reproduced with a discretized representation of the fracture geometry, because all surface features are rectangular with a minimal size equal to a/n. Hence, the growth of the initial contact area is numerically modeled here as a stepwise process with the sudden appearance of new contacts near old ones.

Second, the critical value P_c, at which opposite surfaces of the fracture touch each other at some new contact zones, is determined as explained in Sec. IV. Then, the aperture field b is obtained for three successive values $P=P_c/3$, $2P_c/3$, and P_c. Figure 7(a1) shows the initial aperture field b_{in} of the fracture G_1 and Fig. 7(a2,3,4) shows the difference $b_{\text{in}}-b$ for these values of P. One can see from Fig. 7 that the deformation field is closely related to the initial aperture field of the fracture; the largest deformations are in the zones with largest b_{in} and the smallest ones are near contact zones where b_{in} is minimal.

It can be observed in Fig. 7(a4) that the deformation field at $P=P_c$ is almost uniform. This means that the modified fracture geometry may be approximated by reducing the local fracture aperture b by the closure value ΔV. A detailed analysis of the evolution of the aperture field showed that **d** was less uniform for $b_m/\sigma_h \leqslant 0.5$. This means that for small S_c (or large b_m/σ_h), the fracture surface heights remain normally distributed, which is important for the validity of the nonlinear theory given by Eq. (30) and (32).

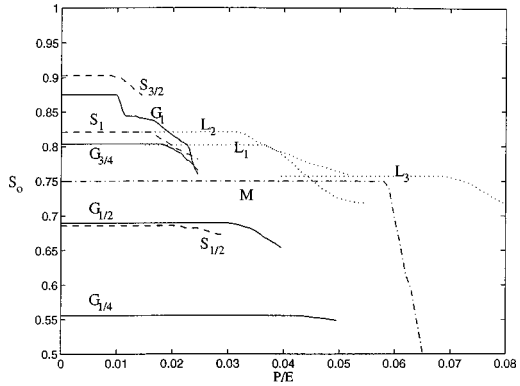

FIG. 8. The fractional void area S_0 as a function of P/E for all fractures. Data are for Gaussian fractures (solid lines), self-affine fractures (dashed lines), step fracture (dashed-dotted line), modified Gaussian (dotted lines).

Large deformations [Figs. 7(b) and 7(c)], after the appearance of new contact zones, were addressed using the scheme presented in Sect. IV B and IV C. For normal loads P larger than P_c, new fracture geometries, referred to as L_1 and L_2, are defined. The new geometry L_2 is taken at $P/E=0.012>P_c/E$, at which several new contacts appeared. In order to restart the calculation procedure, the discretized fracture geometry should be coarsened back to the former $(24)^3$ grid. The error induced by this coarsening can be illustrated by the fact that the contact area S_c and the mean aperture $\langle b\rangle$ calculated on the finer grid are equal to 0.157 and 2.54a, while on the coarse one they are equal to 0.179 and 2.76a, respectively.

The case L_1 corresponds to the modified geometry of G_1 at $P=1.5P_c$ with the initial aperture $\langle b\rangle=2.47a$ on the coarse grid and $\langle b\rangle=2.44a$ on the fine one. The two configurations L_1 and L_2 are compared here, because they represent two possible choices of P/E for the modified geometry; L_1 is constructed with minimal loss in $\langle b\rangle$, regardless of the losses in S_c when the coarsening is performed, while L_2 is constructed so that both $\langle b\rangle$ and S_c would not be changed significantly during the coarsening [cf. Figs. 8 and 9(b)]. Note that L_2 is taken at the beginning of a plateau, which follows an abrupt increase of the contact area (Fig. 8).

Figure 7(b) shows the evolution of the aperture b as a function of P/E for the fracture G_1 with a geometry, modified at $P/E=0.012$ (L_2). Finally, a third geometry L_3 is defined from the deformed state of L_2 at $P/E=0.0415$. Its deformations under further loads are presented in Fig. 7(c). The comparison of the aperture fields shows that new contacts appear near former contact zones in regions of small b. For large P/E, the displacement field **d** becomes less uniform than for $P/E=0$ [Figs. 7(a4) and 7(b4)].

Figure 7(d) presents the aperture distributions for all configurations, G_1, L_1, L_2, L_3, for the same $P/E=0.071$, which corresponds to the critical load P_c for L_3. Comparison shows that the new contacts that appear during the fracture

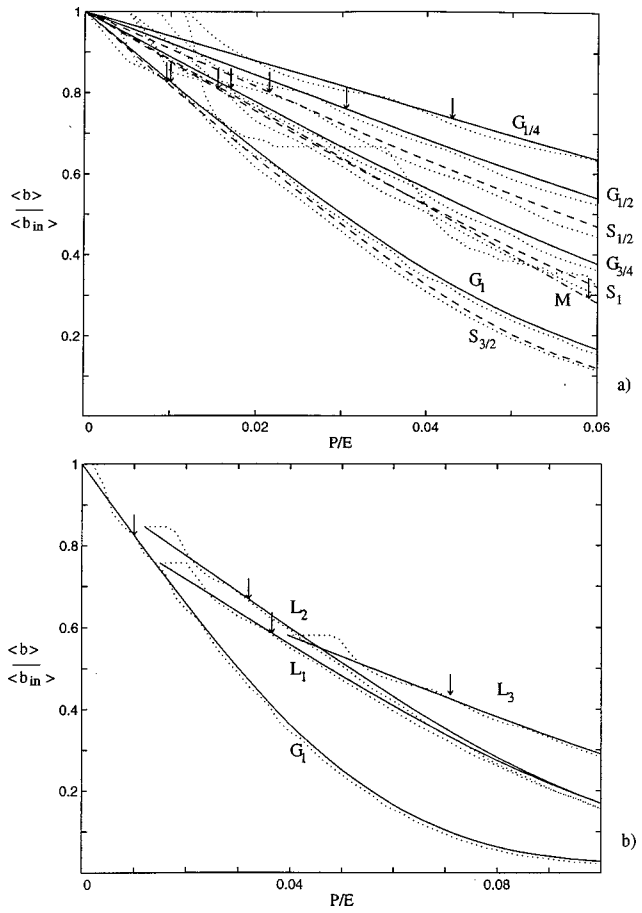

FIG. 9. The relative mean fracture aperture $\langle b\rangle/\langle b_{\rm in}\rangle$ as a function of P/E for all fractures (a) and for the sample G_1 (b). The dotted lines represent $\langle b\rangle/\langle b_{\rm in}\rangle$ obtained by the discrete method. The other lines with the same notation as in Fig. 8 represent the data obtained by the continuous method. The vertical arrows indicate the critical loads P_c.

closure substantially influence the deformation process. The new contacts, which are accounted for in L_1, L_2, L_3, rigidify the fracture, and give lesser closures. The most significant difference is observed between the configurations G_1 and L_3. In the case of G_1, fracture surfaces overlap on an area larger than half of the cell size; the aperture is substantially reduced.

The evolution of the fractional void area $S_0 = 1 - S_c$ of the fracture is presented in Fig. 8 for all the models and for the successive states of G_1. The critical load P_c/E at which new contacts appear is a decreasing function of the initial contact surface S_0; this can be explained by the larger rigidity of fractures with small S_0. The initial plateaus in Fig. 8 become larger when S_0 is decreased for fractures with modified geometries derived from G_1.

B. Evolution of the mean aperture

The mean fracture aperture $\langle b\rangle$ is calculated at various normal loads P in two different ways. First, for each given load P, the modified fracture geometry is reconstructed on a discrete grid and the mean aperture $\langle b\rangle$ is calculated as the number of liquid cubes divided by the total fracture area. This method will be referred to as the discrete method. Second, the continuous method employs the values of ε_S given by Eq. (35). The mean aperture $\langle b\rangle$ is calculated as the sum of $(1-\varepsilon_S)a^3$ over the sample divided by the fracture area.

The curves for $\langle b\rangle$ obtained by the discrete method exhibit a stepwise behavior in contrast with the continuous method. Figure 9 shows $\langle b\rangle/\langle b_{\rm in}\rangle$ versus P/E, obtained by both methods; the difference between them illustrates the error induced by the discretization of the initial fracture geometry.

$\langle b\rangle$ is always found to be a decreasing function of P/E, as physically expected. The variations of $\langle b\rangle/\langle b_{\rm in}\rangle$ become more important when the mean separation b_m/σ_h of the fracture increases, as can be seen for all random fractures in Fig. 9; this means that $\langle b\rangle/\langle b_{\rm in}\rangle|_{P/E} - \langle b\rangle/\langle b_{\rm in}\rangle|_{P/E=0}$ is an increasing function of b_m/σ_h. At large b_m/σ_h, i.e., for $S_c \ll 1$, the deformation of surface asperities and of the solid matrix near the fracture dominates and the decreases of $\langle b\rangle/\langle b_{\rm in}\rangle$ is substantial. For small b_m/σ_h and large S_c, the deformation of the solid above and below the fracture dominates and $\langle b\rangle/\langle b_{\rm in}\rangle$ decreases slowly with P/E.

All curves in Fig. 9 show a nonlinear behavior when P/E increases, though the decrements $\delta h^{\pm}$ of fracture surfaces, as well as the displacement **d**, are linear functions of P. The nonlinearity results from upper and lower surface overlaps, with b set to 0. Arrows in Fig. 9 show the critical normal load P_c/E at which new contacts appear. A very small nonlinearity for $P > P_c$ is visible on the numerical data for the step fracture model, which is caused by the self-overlap of vertical and horizontal parts of fracture surfaces. At $P > P_c$, the calculation of fracture closure V is not valid and the use of the modified fracture geometry at $P \approx P_c$ is required in order to continue the numerical calculation of the fracture deformation.

Figure 9(b) presents the plots of $\langle b\rangle/\langle b_{\rm in}\rangle$ for the sample G_1 obtained by using the modified fracture geometries for loads $P > P_c$. It can be seen that the new contacts significantly influence the evolution of $\langle b\rangle$. The error accumulates with P/E and only the initial parts of the curves in Fig. 9(a) represent the fracture deformations accurately. The curves L_1 and L_2 are not very different from one another. Hence, the real evolution of $\langle b\rangle$ is best approximated by Fig. 9(b) where the maximum value of $\langle b\rangle$ is taken for each P/E.

C. Normal stiffness

The normal joint stiffness k defined by Eq. (10) of real rock fractures depends upon the normal load because of the nonlinear behavior of stress-closure relation of joints. For the small deformations considered here, k is constant until the first overlap of the fracture surfaces.

The closure V defined by the continuous method (cf. Sec. V B) is used to calculate k as the ratio $\delta P/\delta V$ where δP and δV are small increments of the normal load and the corresponding closure of the fracture.

The normal stiffness k is shown in Fig. 10 as a function of the initial contact area S_c for all types of fractures. It is important to recall here that for the same family of fractures, the two initial random surfaces are identical and the average distance between them is changed, thereby modifying the initial surface contact S_c. Since the initial S_c is related to the initial load, this plot may illustrate the effect of the normal load on k. The stiffness increases with S_c, in agreement with

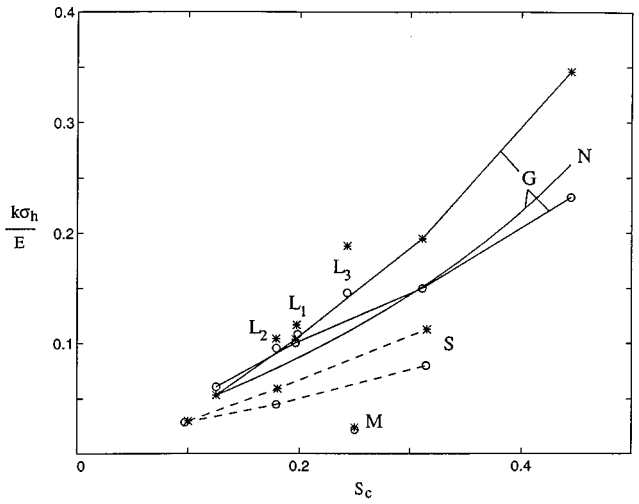

FIG. 10. The dimensionless stiffness $k\sigma_h/E$ as a function of the fractional contact area S_c calculated numerically (*) and by Eq. (28) (○). The solid lines correspond to Gaussian fractures, the dotted lines to self-affine fractures. *M* denotes data for the step fracture. *N* denotes the data obtained by the nonlinear theory [Eqs. (30) and (32)].

some experimental data [11] and numerical results [8].

The various types of fractures considered here show different values of the normal stiffness for the same contact area S_c. According to the mean field theory, only two geometrical parameters, S_c and $\mathcal{L}/\sigma_h$, determine the dimensionless stiffness $k\sigma_h/E$. At $S_c=0.25$, the correlation length $\mathcal{L}/\sigma_h$ is equal to 3.98, 1.3, and 0.7 for the step, the self-affine and the Gaussian fracture, respectively; the difference in $\mathcal{L}/\sigma_h$ seems to be one of the major causes of the observed difference in the fracture stiffness. The parameter $\mathcal{L}/\sigma_h$ is related to the contact number n_c per unit fracture area; n_c is an increasing function of $\mathcal{L}/\sigma_h$ [18]. The fact that the fracture with smaller number of contacts is stiffer agrees with the data of Hopkins *et al.* [8].

k is compared to the theoretical formula (28) in Fig. 10, when the correlation length $\mathcal{L}$ is estimated directly for all samples by using the definition (26). The linear predictions are close to the numerical values of k for the deterministic fracture and at small S_c for the Gaussian and self-affine fractures. The nonlinear theory [Eqs. (28), (30), and (32)] was used in order to find the stiffness of the fracture G_1 when S_c varies from 0.12 to 0.45, which corresponds to the variation of S_c from the initial state of G_1 to the configuration $G_{1/4}$. The results displayed in Fig. 10 show that the nonlinear theory is equivalent to the linear theory for small values of S_c, as it should; when S_c is larger than 0.3, the nonlinear stiffness becomes significantly larger than the linear stiffness and its evolution is parallel to the full numerical computations.

It should be noted that in the case of the step fracture the initial fracture surfaces are planar and that the fracture is symmetric; thus, the two assumptions used in the mean field approximation are exactly fulfilled. The good agreement between the numerical and theoretical data even for $S_c=0.25$ for the step fracture shows that the exact distribution of the normal stresses on the contact surface has little influence.

Figure 10 shows the normal stiffness $k\sigma_h/E$ for Gaussian fractures with various b_m/σ_h and for the sample G_1 obtained by using modified fracture geometries. The numerical points for the two configurations L_1 and L_2, are almost on the same curve as the data for G_1, $G_{3/4}$, and $G_{1/2}$. Since at small P/E the displacement of fracture surfaces for the sample G_1 is uniform, the modified geometry of the fracture at this value of P/E can be obtained by diminishing the distance b_m between the two initial surfaces. When S_c is increased, the displacement becomes nonuniform and the modified fracture L_3 is stiffer than fractures reconstructed by a simple reduction of b_m/σ_h. This means that the dependence of $k\sigma_h/E$ versus S_c obtained by using samples $G_1-G_{1/4}$ only approximates the variation of the fracture stiffness with the normal load for large S_c.

D. Comparison of the normal joint stiffness with data and discussion

Laboratory studies [13,14,5] of the deformation characteristics of rock joints under normal load showed that the closure of joints varies nonlinearly with the normal stress P, whatever the rock and joint types. When P is increased, the joints reach a maximum closure $V_{\max}$. Upon unloading, the joints exhibit hysteresis, which is attributed to friction on parts of the surface where the contact is oblique to the load [21]. This strong nonlinear behavior of rock joints was also obtained by the mean field theory (Sec. III) as displayed in Fig. 3(a). The joint stiffness at various normal loads is a function of the fractional contact area S_c. If the fracture geometries used in the numerical simulations are assumed to represent various initial stress states with various S_c, the corresponding curve $k(S_c)$ can be compared to the experimental data.

Bandis *et al.* [14] studied experimentally the joint deformation characteristics under normal and shear load. They found that the experimental curves $P(V)$ for well interlocked joints can be fitted by a hyperbolic relation [13] and they proposed

$$k=k_0\left(1-\frac{P}{k_0V_m+P}\right)^{-2}, \tag{38}$$

where k_0 is the initial normal stiffness. For dislocated joints obtained by displacing jointed block halves, a linear relation between k and P was found:

$$k=\beta P. \tag{39}$$

Bandis *et al.* [14] estimated the contact area of fractures by inserting a thin plastic sheet between the interlocked joint walls; S_c ranged between 0.4 and 0.7 for various samples at the highest pressure. S_c and $\mathcal{L}$ are calculated here for $P=8$ MPa by using images of the contact area distribution presented for joints compressed in interlocked and mismatched positions. The stiffness k derived from the data of Bandis *et al.* [14] for three types of rocks at the normal load $P=10$ MPa and normalized by $E/\mathcal{L}$ is presented in Fig. 11.

Figure 11 displays also the experimental data of Gentier [11] and Iwai [24]. Gentier studied hydromechanical behavior of well-interlocked fractures in granite and presented a relation between the apparent Young's modulus E_{app} of frac-

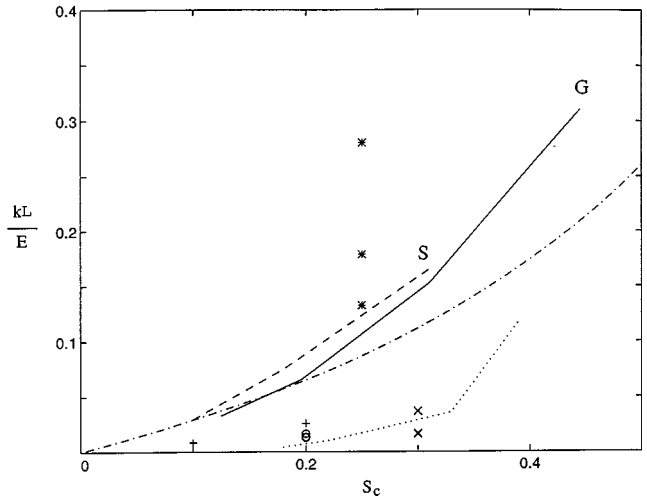

FIG. 11. The joint stiffness k as a function of S_c normalized by $E/\mathcal{L}$. The solid line corresponds to numerical data for the Gaussian fractures, the dashed line to self-affine fractures, the dashed-dotted line to Eq. (28). The experimental data of Gentier [11] correspond to the dotted line; $\times$ and $\bigcirc$ represent the data of Bandis *et al.* [14] for correlated and uncorrelated fractures, $(+)$ corresponds to the data of Iwai [24]. The numerical data of Hopkins *et al.* [8] are denoted by $*$.

tured samples and the normal load P, which is used to estimate the normal stiffness k. The fractional contact area S_c was measured for the same P by inserting a plastic film between fracture surfaces.

The data of Iwai [24] were obtained on samples of basalt, granite, and marble containing well-matched tension fractures. The values of the joint stiffness at $P=10$ MPa are estimated from the slopes of stress-closure curves. S_c measured for the maximum normal load was equal to 0.1–0.2 for granite and to 0.25–0.35 for marble, respectively. These data are presented in Fig. 11, assuming S_c equal to 0.1 and 0.2 for $P=10$ MPa, for granite and marble, respectively. The experimental data are seen to be smaller than the numerical ones in Fig. 11.

Yoshioka and Scholz [25,26] measured closures under normal load in a joint within Westerly granite. The joint was obtained by cutting a rock sample with a fine saw. Two types of cut surfaces were prepared (referred to as ''smooth'' and ''rough'') with different grounding techniques. The surface height distributions are best described by γ distribution functions, from which we may estimate $\sigma_h \approx 2.4$ and 10.5 μm for the smooth and rough surfaces, respectively. These estimates correspond exactly to the geometrical overlap of the two surfaces ($d_i=2.3$ and 10.8 μm) for zero pressure obtained by fitting the results of a theoretical model to the experimental data.

It is very difficult to compare their results to the data in Fig. 11, because the correlation length $\mathcal{L}$ is not known, and because the contact area S_c is quite low. It is estimated as less than 1% for the ''smooth'' joint, under the maximal normal load imposed in the experiments (35 MPa). However, as already mentioned, the contact area is directly related to the confining pressure. Therefore a comparison is made instead in Fig. 3(b) with the predictions of the mean-field analysis of Sec. III, which are in fair agreement with the numerical calculations (see Figs. 10 and 11). The data for the ''smooth'' joint are very close to the prediction (28), although the latter are based on a different height distribution function. The stiffnesses measured on the ''rough'' joint exceed the prediction (28) by a factor of about 2.

Durham and Bonner (1994) considered fractures in the same type of Westerly granite, created in a cylindrical sample by the so-called brezilian technique. Unmated and mated fractures were obtained by reassembling the half samples with or without a transversal offset. We have estimated the surface roughness $\sigma_h \approx \sigma_b/\sqrt{2}$ from their aperture probability distribution for the offset joint. Again, the contact surface area S_c and its correlation length $\mathcal{L}$ are not known accurately. Thus, the joint stiffnesses obtained from their stress-closure plots for the unmated fracture are compared with the mean field predictions in Fig. 3(b). The agreement with the prediction (28) for a self-affine fracture is very good. Of course, the mated joints are much stiffer, and the stiffness coefficients are 2–5 times larger. The same authors also considered joints in different types of rocks: Creighton Gabbro [28] and amphibolite [29]. But again the surface profiles are highly correlated (θ close to 1), and no comparison can be made with the present calculations, restricted to $\theta=0$.

Engelder and Scholz [30] measured permeability and aperture changes within very smooth joints in Cheshire quartzite; samples were saw cut and ground with controlled grits. Their measurements of the normal stiffness coefficient are given in Fig. 3(b). Since the roughness σ_h was not reported, it was taken equal to half the measured ultimate closure.

Boitnott and Scholz [31] defined precisely the concept of effective stress in an attempt to include pore and confining pressures in a single constitutive law for joint closure. Experiments were performed on smooth lapped glass joints and on lapped and fractured rocks; pore and confining pressures could be varied independently. No permeability measurements were performed. Some of their data for ground optical glass with $\sigma_h=13.3$ μm are given in Fig. 3(b). They are similar to the measurements of Yoshioka and Scholz [25,26] on the ''rough'' Westerly granite joints, which have a roughness in the same range.

For the sake of completeness, the numerical results of Hopkins *et al.* [8] are also presented in Fig. 11. Typical values of the normal stiffness $k\mathcal{L}/E$ of two plates separated by disks of height h and diameter D are calculated for the ratio $D/h=8$ (maximum k), 14, and 16 (minimum k). These values are larger than ours and they depend upon D/h.

This comparison shows that the results of the present numerical study of the deformational properties of fractures agree qualitatively with other numerical and experimental results. The difference between the numerical and theoretical data, on one hand, and the experimental results, on the other hand, may be partially attributed to uncertainties in the measurements of fracture parameters. First, the contact area S_c was measured by using plastic films and is possibly overestimated. In this case the experimental points in Fig. 11 should be shifted towards the left side of the plot. Second, the correlation length $\mathcal{L}$ was never measured systematically and its values are only roughly estimated here.

We now discuss the various sources of nonlinearities that are present in the process of fracture loading. The first one is

the variation of the contact area because of progressive closure; the simplest example of this effect is the Herz contact theory [10]. The second one is the fact that plastic deformations certainly occur very rapidly at the top of the asperities. The third one is caused by the identations, i.e., the irreversible damages, induced by loading.

The present satisfactory comparisons with experiments show that the first source is probably predominant in them and that the two other are of a smaller order of magnitude. It should also be noticed that only unmated surfaces were used in the present simulations. This feature could be easily included and it will probably improve the comparisons.

VI. FRACTURE PERMEABILITY

A. Fracture permeability variation with normal stress

In order to analyze the influence of the normal load P on the fracture hydraulic properties, the modified fracture geometry was determined at several levels of P/E for each sample and the permeability tensor $\mathbf{B}_S$ was calculated. Since the discretized fracture geometry does not vary continuously with P/E, $\mathbf{B}_S$ was calculated for the values of P/E, which correspond to the intersections of the curves $\langle b \rangle$ determined by the continuous and the discretized methods [see Fig. 9(a)]. This condition is thought to minimize the influence of the discretization error on the relation between $\langle b \rangle$ and b_S.

The two components B_{Sxx} and B_{Syy} of the permeability tensor [cf. Eq. (4)] are determined and the hydraulic aperture b_S is calculated:

$$b_S = [6(B_{Sxx} + B_{Syy})]^{1/3}. \tag{40}$$

When the sample percolates only in one direction (such as $G_{1/2}$ and $S_{1/2}$), Eq. (40) is still applied with 0 along the direction of no percolation.

The hydraulic fracture aperture b_S normalized by its initial value $b_{S0} = b_S(P=0)$ is shown in Fig. 12(a) as a function of the normal load P/E. The sample $G_{1/4}$ does not percolate even at $P=0$ and is not represented. As expected, the hydraulic aperture b_S decreases with P/E for all fractures. The variations of the mean hydraulic and geometrical apertures are similar; b_S and $\langle b \rangle$ decrease with P/E more rapidly when b_m/σ_h is large [see Fig. 9(a)].

It is interesting to note that the curves b_S/b_{S0} versus P/E are less influenced by b_m/σ_h for the self-affine fractures than for the Gaussian ones; recall that the characteristic length l/σ_h is equal to 6 and 2, for the former and the latter, respectively. Flow simulations in fractures [16] showed that the hydraulic properties are less influenced by b_m/σ_h when l/σ_h is large.

The normalized hydraulic aperture b_S/σ_h is displayed in Fig. 12(b). The dependence upon the flow direction is larger for self-affine fractures than for Gaussian ones. This reflects the fact that the ratio L/l of the sample size and of the correlation length is smaller for the self-affine fractures (see Table I); in this case the results are more influenced by finite size effects.

The variations of b_S/σ_h with P/E for the reconstructed modified fracture geometries L_1, L_2, and L_3 are gathered in Fig. 12(b). The absolute value of the slope decreases with P/E in agreement with experiments [32,11]. This behavior is

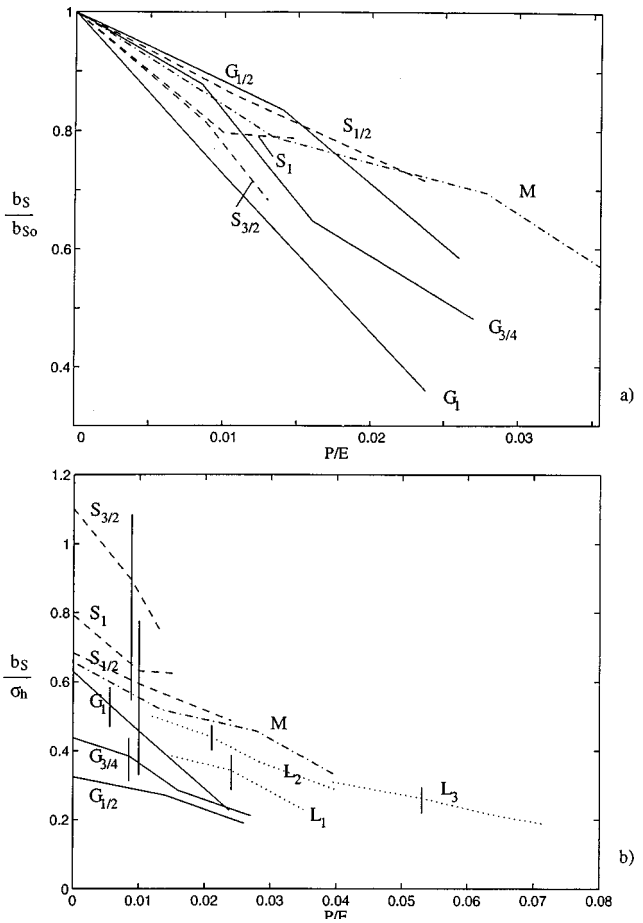

FIG. 12. The mean hydraulic aperture b_S/b_{S0} (a) and b_S/σ_h (b) as functions of P/E. The vertical bars represent the variations of b_S with the direction of the mean pressure gradient.

analogous to the variations of $\langle b \rangle/\sigma_h$ with P/E [Fig. 9(b)]; for small P/E, the deformation of the fracture itself is predominant and induces a rapid decrease of b_S/σ_h; at large enough P/E, the deformation of the solid above and below the fracture is predominant and b_S/σ_h slowly varies with P/E.

B. Fracture permeability variation with the mean aperture

An alternative presentation of the same results is given in Fig. 13 where b_S/σ_h is displayed as a function of $\langle b \rangle/\sigma_h$. The various data are efficiently gathered in this plot, which can be approximated by the linear relation

$$\frac{b_S}{\sigma_h} = \alpha \frac{\langle b \rangle}{\sigma_h} + \beta, \tag{41}$$

where α is close but not equal to 1 (see Table III). If the relation (41) is extrapolated towards $b_S = 0$, the ratio $-\beta/\alpha$ may be considered as a critical aperture $\langle b \rangle_c/\sigma_h$ at which the fracture does not percolate. Table III gives $-\beta/\alpha$ for all fractures. This ratio decreases with decreasing initial separation b_m/σ_h of fractures ($G_1 - G_{1/2}$, $S_{3/2} - S_{1/2}$). The value of $-\beta/\alpha$ substantially decreases when the fracture is submitted to the large deformations (G_1, L_2, L_3). This means that due to the increasing stiffness, the fracture remains open and the fluid can flow even for small $\langle b \rangle/\sigma_h$. The numerical results

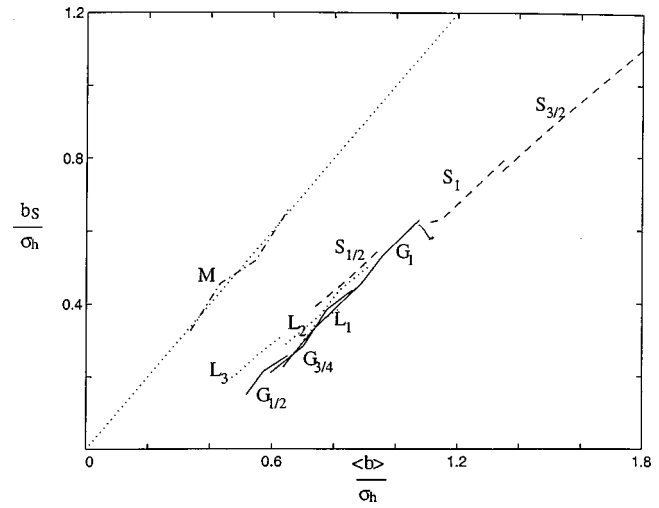

FIG. 13. The mean hydraulic aperture b_S/σ_h as a function of $\langle b\rangle/\sigma_h$. Same conventions as in Fig. 8. The diagonal dotted line corresponds to $b_S=\langle b\rangle$.

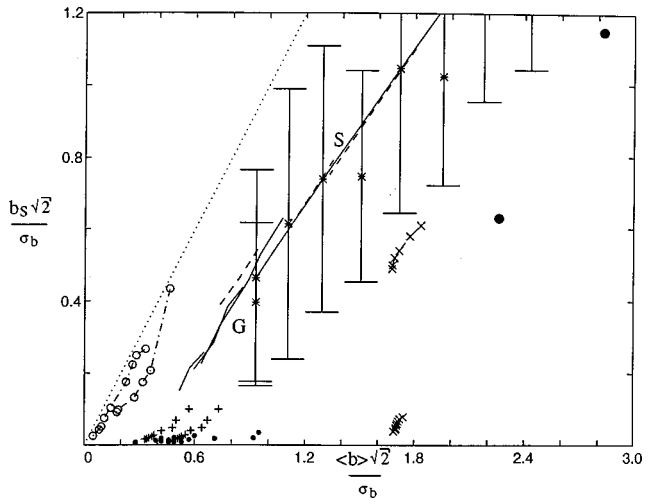

FIG. 14. The hydraulic aperture b_S as a function of the mean aperture $\langle b\rangle$ normalized by $\sqrt{2}\sigma_b$. The solid line corresponds to the numerical data for Gaussian fractures, the dashed line to the self-affine fractures. The dotted line represents $b_S=\langle b\rangle$. The experimental data of Gentier [11] and Gale [22] are denoted by $\times$ and $\bigcirc$, respectively. The $\bullet$ refer to Durham and Bonner's [27] measurements in an unmated Westerly granite joint. Durham [29] data for an amphibolite joint $(+)$ are given for two reasonable guesses for the initial aperture. The smaller black dots are the data of Kranz *et al.* [34] for Barre granite. The numerical data of Mourzenko *et al.* [18] are denoted by $*$. The vertical bars represent the standard deviation of b_S due to the statistical scatter of the data.

only approximately verify the standard ''cubic law'' [33] which relates the hydraulic and the mean apertures of the fracture. This is also true for the large deformations of the fracture G_1 (cf. Fig. 13); the value α decreases from $0.91(G_1)$ to $0.81(L_2)$ and $0.72(L_3)$.

C. Hydraulic aperture as a function of mean aperture

Experimental studies of the hydromechanical behavior of fractures under a normal load P [11,22,24] showed that a nonlinear relation is obtained between the hydraulic fracture aperture b_S and P, which can be associated with the nonlinearity of the dependence of V upon P/E. The experimental data of Gentier [11,22] and Gale [22] are displayed in Fig. 14. Both apertures, b_S and $\langle b\rangle$, are normalized by the experimental value $\sigma_b\sqrt{2}$.

Fractures studied by Gentier [11] had highly correlated surfaces with $\theta\approx 0.99$ and their hydraulic properties are seen to be very sensitive to the geometrical characteristics. The experimental points are far from the curve for the pure Poiseuille flow $b_S=\langle b\rangle$. The data of Gale [22] are less influenced by the fracture roughness and they better agree with the theoretical prediction $b_S=\langle b\rangle$. The permeabilities measured by Durham and Bonner [27] in an unmated Westerly granite joint under 80 and 160 MPa normal loads ($P/E=1.9\times10^{-3}$ and 3.7×10^{-3}) are much larger than in the corresponding mated joint (hydraulic aperture close to zero, not represented). The amphibolite joint investigated by Durham [29] is also highly correlated. The initial mean aperture is not known accurately. Two plots are proposed in Fig. 14, by assuming $\langle b_{\rm in}\rangle=120\ \mu$m (the upper bound for $\langle b\rangle$ at $P=0$ mentioned by the authors) and $\langle b_{\rm in}\rangle=100\ \mu$m. One can see that the numerical curves b_S versus $\langle b\rangle$ also presented in Fig. 14 exhibit the same trend as the experimental results.

TABLE III. The coefficients α and β of the relation (41) for various fractures.

Sample name	α	$-\beta$	$-\beta/\alpha$
G_1	0.91	0.35	0.38
$G_{3/4}$	0.90	0.33	0.37
$G_{1/2}$	0.79	0.25	0.32
L_1	0.92	0.35	0.38
L_2	0.81	0.24	0.30
L_3	0.72	0.14	0.19
$S_{3/2}$	0.74	0.23	0.31
S_1	0.73	0.20	0.27
$S_{1/2}$	0.75	0.16	0.21
M	1.00	0.003	0.003

Kranz *et al.* [34] measured the permeability of Barre granite, which was saw cut and ground with various controlled grits. Changes in permeability were found to vary linearly with pore and confining pressures that could be varied independently. Only a few data are given on aperture variations with pressure. Some of their permeability measurements (from their Table II) are plotted in Fig. 14.

Figure 14 presents also the numerical data of Mourzenko *et al.* [16] obtained for self-affine fractures. Each data point is the average over 10 realizations of the fracture surfaces. One can see that the hydraulic aperture b_S of the fractures submitted to normal load follows the similar linear dependence as the value b_S averaged over statistically independent realizations of fractures with corresponding mean $\langle b\rangle$. The results of the present numerical calculations are within the interval of statistical scatter of the data.

Comparison shows good agreement between numerical and experimental data. All curves represent a similar dependence of hydraulic properties of fractures upon the geometrical ones.

VII. CONCLUSIONS

The macroscopic mechanical and hydraulic properties of fractures with rough surfaces were analyzed by solving numerically the local three-dimensional equations. The solid matrix is assumed to be an elastic solid described by the classical Lamé coefficients. The flow through the fracture is analyzed by solving the Stokes equations. The full deformation history of the fracture is represented as a series of steps with the successive appearance of new contact zones.

Three types of fractures were addressed in this paper, namely, a step deterministic fracture and two fractures with random normally distributed surface heights and with Gaussian and self-affine spatial correlations. The dependences of the mean aperture $\langle b \rangle$ and of the hydraulic aperture b_S upon the applied normal load P were analyzed. The variations of $\langle b \rangle / \langle b_{\rm in} \rangle$ and b_S / b_{So} were found to be more important when the mean separation b_m / σ_h of the fracture increases; the hydraulic properties of the fractures follow the mechanical ones.

The normal joint stiffness k of a fracture was analyzed as a function of the initial contact area S_c. The experimental stiffness of the real rock joints is smaller then the numerical one, but the relations $k(S_c)$ are qualitatively similar.

The relation between the numerical values of the hydraulic aperture b_S and the mean aperture $\langle b \rangle$ is similar to the ones derived from published laboratory experiments. The hydraulic properties of fractures are substantially influenced by the surface roughness.

A mean field analysis of the deformation of the fracture surfaces provides a formula of the normal joint stiffness as a function of the geometrical parameters of the fracture and of the mechanical properties of the solid matrix. The numerical results are in good agreement with the mean field theory, especially for small S_c.

No substantial influence of the type of the spatial correlations on the macroscopic mechanical and hydraulic properties was found. However, final quantitative conclusions will be reached only when systematic calculations are performed on a large series of fractures of the same type. The extensions of this work to macroscopic tangential stresses is in progress.

ACKNOWLEDGMENT

Most computations were performed at CNUSC (subsidized by the MESR) whose support is gratefully acknowledged.

APPENDIX: DERIVATION OF THE JOINT STIFFNESS IN THE MEAN FIELD APPROXIMATION

The covariance function $R_c(t)$ of the random field $Z_c(\mathbf{r})$ defined by Eq. (24) can be derived from the covariance function $C_h(t)$ of the fracture surface height $h(\mathbf{r})$. Because of ergodicity, $R_c(t)$ can be written as

$$R_c(t) = \frac{1}{S_c(1-S_c)} \langle (Z_c(\mathbf{0}) - \overline{Z_c})(Z_c(\mathbf{t}) - \overline{Z_c}) \rangle. \quad \text{(A1)}$$

An equivalent form of the definition (24) is

$$Z_c(\mathbf{r}) = \begin{cases} 1, & w < 0 \\ 0 & w \geqslant 0, \end{cases} \quad \text{(A2)}$$

where $w = h^+ - h^-$ is a Gaussian field with mean b_m and standard deviation $\sqrt{2}\sigma_h$. Introduction of Eq. (A2) into (A1) yields

$$\langle (Z_c(\mathbf{0}) - \overline{Z_c})(Z_c(\mathbf{t}) - \overline{Z_c}) \rangle = \int_{-\infty}^{0} dw_1 \int_{-\infty}^{0} dw_2 \; \varphi(w_1, w_2) - S_c^2,$$

$$w_1 = w(\mathbf{0}), \quad w_2 = w(\mathbf{t}), \quad \text{(A3)}$$

where $\varphi(w_1, w_2)$ is the joint distribution of the Gaussian variables

$$\varphi(w_1, w_2) = \frac{1}{4\pi\sigma_h^2\sqrt{1-\gamma^2}} \exp\left[- \frac{(w_1 - b_m)^2 - 2\gamma(w_1 - b_m)(w_2 - b_m) + (w_2 - b_m)^2}{4\sigma_h^2(1-\gamma^2)} \right],$$

$$\gamma = \frac{C_h(t)}{\sigma_h^2}. \quad \text{(A4)}$$

The first term in the right-hand side of the Eq. (A3) can be calculated by using the transformation

$$w_1 = b_m - 2\sigma_h x,$$

$$w_2 = b_m - 2\sigma_h(\gamma x + \sqrt{1-\gamma^2} y)$$

$$\int_{-\infty}^{0} dw_1 \int_{-\infty}^{0} dw_2 \; \varphi(w_1, w_2) = \frac{2}{\pi} \int_{b_m/2\sigma_h}^{+\infty} dx \int_{\alpha x}^{+\infty} dy \; e^{-x^2 - y^2},$$

$$\alpha = \sqrt{(1-\gamma)/(1+\gamma)}. \quad \text{(A5)}$$

Use of the distribution (15) for w implies

$$S_c=\frac{1}{\sqrt{\pi}}\int_{b_m/2\sigma_h}^{+\infty}e^{-x^2}dx. \tag{A6}$$

The correlation function $R_c(t)$ can be written as

$$R_c(t)S_c(1-S_c)=\frac{2}{\pi}\int_{b_m/2\sigma_h}^{+\infty}dx\int_{\alpha x}^{x}dy\ e^{-x^2-y^2}. \tag{A7}$$

The definition (26) of the correlation length yields

$$S_c(1-S_c)\mathcal{L}=\frac{1}{2\pi}\int_0^1 T(\gamma)\,\frac{\exp[-b_m^2/2\sigma_h^2(1+\gamma)]}{\sqrt{1-\gamma^2}}\,d\gamma, \tag{A8}$$

where $T(\gamma)$ is the inverse of the correlation function $\gamma(t)$.

When the covariance function $C_w(t)$ is described by the Gaussian (17) or by the self-affine covariance (18), the correlation length $\mathcal{L}$ becomes

$$\mathcal{L}=\frac{l\Psi_\tau(S_c)}{S_c(1-S_c)},\quad \tau=G,s, \tag{A9}$$

$$\Psi_G(S_c)=\frac{1}{2\pi}\int_0^1\sqrt{-\ln\gamma}\,\frac{\exp[-b_m^2/2\sigma_h^2(1+\gamma)]}{\sqrt{1-\gamma^2}}\,d\gamma,$$

$$\Psi_s(S_c)=\frac{1}{2\pi}\int_0^1(1-\gamma)^{1/2\zeta}\,\frac{\exp[-b_m^2/2\sigma_h^2(1+\gamma)]}{\sqrt{1-\gamma^2}}\,d\gamma, \tag{A10}$$

where indices G and s correspond to Gaussian and self-affine fractures.

The expressions (A7) and (A10) can be simplified in the two opposite limits, $b_m/\sigma_h\to 0$ and $b_m/\sigma_h\to\infty$. For small b_m/σ_h (or $S_c\approx 0.5$), the correlation function $R_c(t)$ becomes

$$R_c(t)\approx\frac{2}{\pi}\arcsin\gamma+\frac{2b_m^2}{\pi\sigma_h^2}\left[\frac{2}{\pi}\arcsin\gamma-1+\left(\frac{1-\gamma}{1+\gamma}\right)^{1/2}\right]. \tag{A11}$$

The coefficients Ψ_s and Ψ_G are

$$\Psi_G\approx C_1-\frac{b_m^2}{2\sigma_h^2}C_2,\quad C_1\approx 0.170,\quad C_2\approx 0.034,$$

$$\Psi_s\approx C_1^*-\frac{b_m^2}{2\sigma_h^2}C_2^*,\quad C_1^*\approx 0.129,\quad C_2^*=0.019, \tag{A12}$$

where Ψ_s is found for $\zeta=0.5$.

At large b_m/σ_h, the leading term of the asymptotic representation of $R_c(t)$ is

$$R_c(t)\approx\frac{4\sigma_h^2}{\sqrt{\pi}\alpha(1+\alpha^2)b_m^2}\exp\left[-\frac{b_m^2(1-\gamma)}{4\sigma_h^2(1+\gamma)}\right]. \tag{A13}$$

This formula is valid for $b_m/\sigma_h\gg 1$ and $b_m\alpha/\sigma_h\gg 1$. For large b_m/σ_h, but small $b_m\alpha/\sigma_h$, $R_c(t)$ is

$$R_c(t)\approx 1-\frac{b_m}{\sigma_h}\left(\frac{1-\gamma}{\pi(1+\gamma)}\right)^{1/2}. \tag{A14}$$

The coefficient Ψ_s is represented for $b_m/\sigma_h\gg 1$ as

$$\Psi_s\approx D_1^*\left(\frac{2\sigma_h}{b_m}\right)^{1/2\zeta}\exp\left[-\frac{b_m^2}{4\sigma_h^2}\right],\quad D_1^*=\frac{\Gamma(1/\zeta)}{\sqrt{\pi}2^{1/2\zeta}\Gamma(1/2\zeta)}, \tag{A15}$$

where $D_1^*\approx 1$ for $\zeta=0.5$; Γ is the classical Euler gamma function. For a Gaussian covariance, Ψ_G is expressed as Ψ_s for $\zeta=1$:

$$\Psi_G\approx\frac{4\sigma_h^2}{\pi\sqrt{2}b_m^2}\exp\left[-\frac{b_m^2}{4\sigma_h^2}\right]. \tag{A16}$$

These formulas can be used together with the relation between the mean area S_c and b_m/σ_h for $b_m/\sigma_h\gg 1$;

$$S_c\approx\frac{\sigma_h}{b_m\sqrt{\pi}}\exp\left(-\frac{b_m^2}{4\sigma_h^2}\right) \tag{A17}$$

in order to analyze the variation of the normal fracture stiffness k given by Eqs. (28) and (A9) with the contact area S_c.

[1] J. A. Greenwood and J. B. P. Williamson, Proc. R. Soc. London, Ser. A **295**, 300 (1966).
[2] A. F. Gangi, Int. J. Rock Mech. Min. Sci. **15**, 249 (1978).
[3] Y. W. Tsang and P. A. Witherspoon, J. Geophys. Res. **86**, 9287 (1981).
[4] J. B. Walsh and M. A. Grosenbaugh, J. Geophys. Res. **84**, 3532 (1979).
[5] S. R. Brown and C. H. Scholz, J. Geophys. Res. **90**, 5531 (1985).
[6] S. R. Brown and C. H. Scholz, J. Geophys. Res. **91**, 4939–4948 (1986).
[7] S. R. Brown, J. Geophys. Res. **92**, 1337 (1987).
[8] D. L. Hopkins, N. G. W. Cook, and L. R. Myer, in *Rock Joints* (Balkema, Rotterdam, 1990), pp. 203–210.
[9] A. J. A. Unger and C. W. Mase, Water Res. Res. **29**, 2101 (1993).
[10] L. Landau and E. M. Lifshitz, *Theory of Elasticity* (Pergamon, Oxford, 1970).
[11] S. Gentier, thèse de Doctorat d'Etat, 1986, Université d'Orléans (unpublished).
[12] R. E. Goodman, L. Taylor, and T. L. Brekke, J. Soil Mech. Found. Div. **3**, 637 (1968).
[13] R. E. Goodman, *Methods of Geological Engineering in Discontinuous Rock* (West, New York, 1976), p. 472.
[14] S. C. Bandis, A. C. Lumsden, and N. K. Barton, Int. J. Rock Mech. Min. Sci. **20**, 249 (1983).

[15] L. J. Pyrak-Nolte, L. R. Myer, N. G. W. Cook, and P. A. Witherspoon (unpublished).
[16] V. V. Mourzenko, J.-F. Thovert, and P. M. Adler, J. Phys. (France) II **5**, 465 (1995).
[17] P. M. Adler, *Porous Media: Geometry and Transports* (Butterworth/Heinemann, Stoneham, MA, 1992), p. 544.
[18] V. V. Mourzenko, J.-F. Thovert, and P. M. Adler, Phys. Rev. E **53**, 5606 (1996).
[19] A. Hansen, E. L. Hinrichsen, and S. Roux, Phys. Rev. Lett. **66**, 2476 (1991).
[20] K. J. Måløy, A. Hansen, E. L. Hinrichsen, and S. Roux, Phys. Rev. Lett. **68**, 213 (1993).
[21] C. H. Scholz and S. H. Hickman, J. Geophys. Res. **88**, 6501 (1983).
[22] J. E. Gale (unpublished).
[23] J. Poutet, D. Manzoni, F. Hage-Chehade, C. J. Jacquin, M. J. Boutéca, J.-F. Thovert, and P. M. Adler, Int. J. Rock Mech. Mining Sci. **33**, 409 (1996).
[24] K. Iwai, Ph.D. thesis, University of California, 1976 (unpublished), p. 208.
[25] N. Yoshioka and C. H. Scholz, J. Geophys. Res. **94**, 17 681 (1989).
[26] N. Yoshioka and C. H. Scholz, J. Geophys. Res. **94**, 17 691 (1989).
[27] W. B. Durham and B. P. Bonner, J. Geophys. Res. **99**, 9391 (1994).
[28] W. B. Durham and B. P. Bonner, in *Fractured and Jointed Rock Masses*, edited by L. R. Myer, N. G. W. Cook, R. E. Goodman, and L. F. Tsang (Balkema, Rotterdam, 1995), pp. 441–446.
[29] W. B. Durham (unpublished).
[30] T. Engelder and C. H. Scholz, in *Mechanical Behavior of Crustal Rocks*, American Geophysical Union Monograph No. 24, edited by N. L. Carter *et al.* (AGU, Washington D.C., 1981), pp. 147–152.
[31] G. N. Boitnott and C. H. Scholz, J. Geophys. Res. **95**, 19 279 (1990).
[32] J. E. Gale (unpublished).
[33] P. A. Witherspoon, J. S. Y. Wang, K. Iwai, and J. E. Gale, Water Res. Res. **16**, 1016 (1980).
[34] R. L. Kranz, A. D. Frankel, T. Engelder, and C. H. Scholz, Int. J. Rock Mech. Min. Sci. Geomech. Abstr. **16**, 225 (1979).